Earthquake Engineering & Structural Dynamics
The Journal of the International Association for Earthquake Engineering

EARTHQUAKE ENGINEERING & STRUCTURAL DYNAMICS
Earthquake Engng Struct. Dyn. 2015; **44**:2015–2033
Published online 24 February 2015 in Wiley Online Library (wileyonlinelibrary.com). DOI: 10.1002/eqe.2571

Dimensionless fragility curves for rocking response to near-fault excitations

Elias G. Dimitrakopoulos*,† and Themelina S. Paraskeva

Department of Civil and Environmental Engineering, The Hong Kong University of Science and Technology, Kowloon Bay, Hong Kong

SUMMARY

This paper assesses the seismic fragility of single degree of freedom rocking structures within a probabilistic framework. The focus is on slender rigid structures that exhibit negative stiffness during rocking. The analysis considers ground motions with near-fault characteristics, either solely coherent pulses or synthetic ground motions that include, in addition, a stochastic high-frequency component. The study offers normalized fragility curves that estimate the overturning tendency, as well as the peak response rotation of a rocking structure. It shows that the use of bivariate intensity measures (IMs) can lead to superior fragility curves compared with conventional univariate IMs. Regardless, the study advocates the use of dimensionless–orientationless IMs that offer an approximately 'universal' description of rocking behavior/fragility, a normalized description almost indifferent to the amplitude and the predominant frequency of the excitation or the size and the slenderness of the rocking structure. Importantly, the analysis unveils hidden order in rocking response. There exists a critical peak ground acceleration, below and above which, peak rocking response scales differently. In particular, when the structure does not overturn, the peak rotation follows approximately a biplanar pattern with respect to the intensity and the predominant frequency of the excitation. Finally, the analysis verifies that rocking overturning depends primarily on the velocity characteristics of the ground motion.

Received 31 August 2014; Revised 30 January 2015; Accepted 1 February 2015

KEY WORDS: rocking; overturning risk; fragility curves; rocking bridges; earthquake engineering

1. INTRODUCTION

This paper derives from a broader study [1–3] on the dynamics of rocking structures, which aims to examine the potential merits of rocking behavior as a seismic isolation technique for contemporary structures. Rocking isolation relies on utilizing the rotational inertia of (part of) the structure through purposely activated dynamic motion (primarily rigid body rotations). This is a radically different concept than conventional seismic design that regards dynamic motion as an 'unpleasant' by-product of structural deformation. Rocking behavior is one of the reasons many ancient structures survived millennia in earthquake-prone regions [4,5]. Still, it was only in the 1970s that pioneer engineers rediscovered the value of rocking isolation for contemporary structures [6, 7], and currently, it is proliferating for example in [8] and references therein.

The present study focuses on slender rigid structures that exhibit pure rocking behavior (without sliding) during seismic excitation. The dynamics of such rocking structures differs fundamentally from the dynamics of (conventional) deforming structures. The comparison of the two archetypal systems is as follows: the rocking block and the elastic oscillator [9, 10] encapsulate many of the distinct

*Correspondence to: Elias G. Dimitrakopoulos, Department of Civil and Environmental Engineering, The Hong Kong University of Science and Technology, Kowloon Bay, Hong Kong.
†E-mail: ilias@ust.hk

qualitative differences. A peculiar characteristic of rocking dynamics is the negative stiffness that prevents the structure from resonance under constant frequency (e.g., harmonic) excitation [11]. However, the negative stiffness renders also rocking structures inherently unstable and very sensitive to the characteristics of ground motion. The boundaries between the safe and overturning areas of the control plane (i.e., 'overturning plots') under harmonic loading exemplify this sensitivity (e.g., [12–14]). Further, rocking structures are particularly vulnerable to coherent pulse-type ground motions [15]. Following the seminal work of Housner [15], several publications focused on the prediction of pure-rocking overturning under pulse-type excitations, shedding light on the transient rocking dynamics via deterministic methods [16, 17]. Building on their work, the studies of Dimitrakopoulos [2] and Voyagaki *et al.* [18, 19] offered analytical closed-form solutions for mathematical (pulse-type) ground motion excitations. Still, the presence of multiple impulses, coexisting in the ground motion, can either amplify or deamplify the rocking response perplexing further the problem [10, 11]. More recently, DeJong and Dimitrakopoulos [1] offered a methodology to derive an exact or approximate dynamic equivalency between a variety of rocking structures and the archetypal rocking block.

Even though it is hard to overstate the significance of deterministic methods in elucidating rocking behavior, the frail rocking dynamics remains elusive and difficult to predict. More so, if one considers the inherent uncertainty related to the specific characteristics of future ground motions. Interestingly, in his 1963 paper, Housner [15] tackled the problem also from a stochastic perspective, estimating the probability of overturning via an energy balance equation (see also [20]). Almost two decades later, researchers were confronting typical traits of nonlinear dynamics in rocking response (e.g., [21]); small changes in size, slenderness, or ground motion could cause drastic differentiation of the response. This prompted the prediction of rocking overturning via probabilistic methods: Spanos and Koh [22] deployed a stochastic linearization technique, Cai *et al.* [23] assessed the reliability of a rigid block against toppling under nonstationary and nonwhite (random process) base excitations, and Shao and Tung [24] estimated the overturning probability of a rigid body subjected to real earthquake records. Meanwhile, in the field of earthquake engineering, as the idea of assessing seismic performance via probabilistic methods matured [25], it led to representing the conditional probability of failure (i.e., fragility) of a structure under uncertain input, via pertinent fragility curves (e.g., [26]). Focusing on rocking, Kafle *et al.* [27] developed overturning fragility curves, for unrestrained blocks, based on physical and numerical experiments, while Roh and Cimellaro [28] and Deng *et al.* [29] offered fragility curves for frames with rocking columns ([30]) and bridges with rocking foundations, respectively.

Yet, with a view to use rocking in practical engineering design, a question that persists is that of the seismic reliability of rocking behavior. Motivated by the growing interest in rocking, this study acknowledges the need to tackle the non-predictability of the rocking response probabilistically. To this end, it integrates two different components: (i) a 'universal' description of rocking response from the work in [2] and (ii) a probabilistic framework, borrowed primarily from two recent studies on rocking structures: Psycharis *et al.* [31] and Acikgoz and DeJong [10]. The particular goal of the work reported herein is to assess the seismic reliability of (negative stiffness) rocking structures to near-fault excitations. In this context, the study characterizes, for the first time, the different sensitivity of rocking response to excitations with different amplitude and/or frequency content. In the process, it discusses the effect of the high-frequency component on rocking behavior and contributes towards improved, specialized intensity measures (IMs) for rocking.

2. PROBABILISTIC SEISMIC DEMAND ANALYSIS

2.1. Stochastic model for near-fault ground motions

There are two main choices when selecting ground motions to assess the seismic reliability of a structure: the use of either natural/historic records (e.g., [10]) or synthetic ground motions (e.g., [31]). Because the available natural records with coherent pulses are limited, we employ a probabilistic approach [32, 33] and generate synthetic ground motions. The premise of the adopted methodology is that the low-frequency (long period) and high-frequency components of the ground motion are modeled independently. The long-period component is simulated as a coherent wavelet (Section 2.1.1),

DOI: 10.1002/eqe

whereas the high-frequency component is constructed according to the stochastic method of Boore [34] (Section 2.1.2). In a subsequent stage (Section 2.1.3), the two components are combined to yield a synthetic ground motion (henceforth combined synthetic ground motion (CSGM)) acceleration time history.

For economy of space, we keep the presentation of the method (Section 2.1) short, as it is described in detail in [32, 33] and references therein.

2.1.1. Low-frequency (coherent) pulse. The well-established Mavroeidis and Papageorgiou (M&P) [35] wavelet simulates the coherent long-period component of the CSGM. Its velocity time-history expression is as follows:

$$\dot{u}_p = \begin{cases} \frac{A}{2}\left[1+\cos\left(\frac{\omega_p}{\gamma_p}\left(t-t_0\right)\right)\right]\cos\left(\omega_p\left(t-t_0\right)+v_p\right), t \in \left[t_0-\frac{\pi\gamma_p}{\omega_p}, t_0+\frac{\pi\gamma_p}{\omega_p}\right] \\ 0 \qquad\qquad otherwise \end{cases} \tag{1}$$

where A, ω_p, v_p, γ_p, and t_0 describe the velocity amplitude of the envelope of the pulse, the angular frequency, the phase angle, the oscillatory character (i.e., number of half cycles), and the time shift to specify the epoch of the envelopes peak, respectively. T_p $(= 2\pi/\omega_p)$ is the prevailing period of the pulse. Note that V_p is not in general equal to the envelop amplitude A, but one can be calculated from the other if the phase angle v_p is known.

For every earthquake moment magnitude M_w and epicentral distance from the fault R_e, the mean value of the velocity amplitude V_p in centimeters/second and the corresponding mean value of the period T_p in s are obtained from [36]:

$$\log\left(V_p\right) = -5.17 + 1.98M_w - 0.14M_w^2 - 0.10\log\left(R_e^2 + 0.562\right) \tag{2}$$

and

$$\log\left(T_p\right) = -2.87 + 0.47M_w \tag{3}$$

where log denotes the base 10 logarithm and Equation (2) holds for $M_w \leqslant 7.0$; for higher values $(M_w > 7.0)$, M_w is taken as 7.0 [31].

The magnitude M_w ranges from 5.5 to 7.5 with a step of 0.5 (i.e., five values), and the epicentral distance R_e varies from 5 to 20 km with a step of 2.5 km (i.e., seven values) [31]. For each of the 35 $M_w - R_e$ scenarios, the Latin hypercube sampling [37] procedure generates 100 samples of the (random variables) V_p, T_p, v_p, and γ_p. The pertinent M&P pulses are then constructed with Equation (1). We assume that the logarithms of V_p and T_p follow a normal distribution with standard deviation equal to 0.16 and 0.18, respectively [31], and that γ_p and v_p follow also a normal distribution with mean values 1.93 and 1.83 and corresponding standard deviations 0.47 and 0.98, accordingly [38]. The distribution of γ_p is left truncated to 1 [31].

2.1.2. High- frequency (stochastic) component. To model the high-frequency (>0.1–0.2 Hz) component (henceforth HFC) of the excitations, we adopt the point source stochastic method [34]. The method uses a parametric description of the ground motion's radiation spectrum, which is a product of quantities that consider the effect of source, path, site, and instrument (or type) of motion. The duration of the ground motion is incorporated through an envelope function. Both the radiation spectrum and the duration of the ground motion depend on M_w and R_e. The particular parameters used herein are taken from the Atkinson and Silva [39] study.

2.1.3. Combined synthetic ground motions. The superposition of the previous two components (the coherent M&P pulse of Section 2.1.1 and the stochastic HFC of Section 2.1.2) constitutes the CSGM. The distinct steps of the superposition procedure are described in detail in [31–33]. Overall, the model parameters consist of the seismological parameters M_w and R_e, the additional parameters for the

DOI: 10.1002/eqe

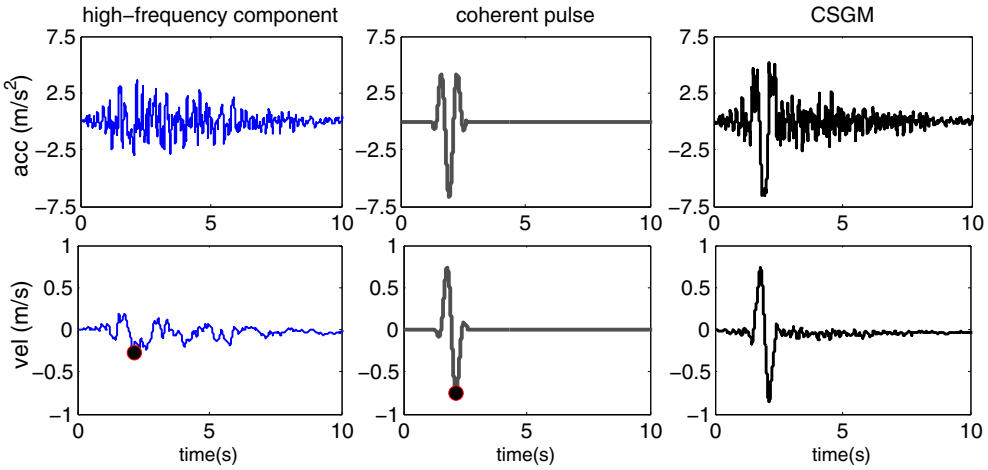

Figure 1. Sample of a combined synthetic ground motion (CSGM): high-frequency component (first column), long-period pulse (second column). Acceleration time history (first row) and velocity time history (second row).

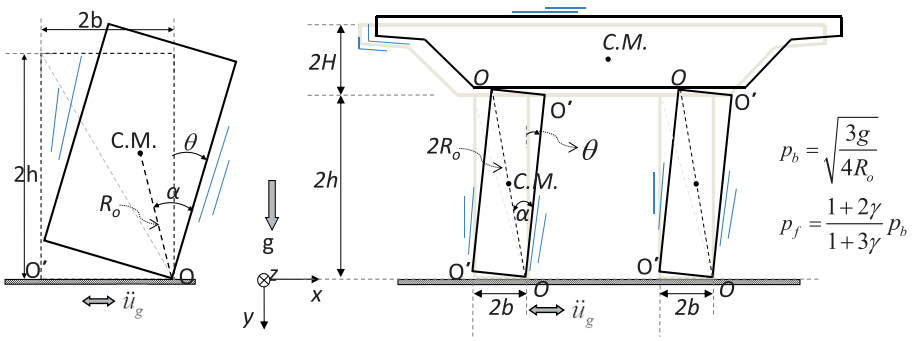

Figure 2. Examined rocking structures: the simple rocking block (left) and the rocking frame (right).

velocity pulse $(V_p, T_p, \upsilon_p, \gamma_p)$, and the white noise sequence [32, 33]. Figure 1 illustrates the two components, as well as the final (sample) CSGM. All simulations for Section 2.1 are performed using MATLAB [37].

2.2. *Structural/seismic response analysis*

2.2.1. Equations of motion. This section summarizes the equations of pure rocking motion: the rigid body rotation about alternate pivoting points (O and O' in Figure 2). Figure 2 presents two single degree of freedom rocking structures: the rocking block (left) and the rocking frame (right) subjected to a horizontal ground motion with acceleration time history $\ddot{u}_g(t)$. The equations of motion describing the pure rocking behavior of these two structures (Figure 2) are identical [1, 40]:

$$\ddot{\theta} = -p^2 \left(\sin\left[\alpha \mathrm{sgn}\left(\theta\right) - \theta\right] + \frac{\ddot{u}_g}{g} \cos\left[\alpha \mathrm{sgn}\left(\theta\right) - \theta\right] \right) \tag{4}$$

where sgn() is the (standard) sign function and p is the rocking frequency parameter. Figure 2 gives the frequency parameter of a rectangular block $p = p_b$ and of a rocking frame $p = p_f$ [40], where γ is the beam-to-columns mass ratio, R_o is the semi-diagonal, and α is the slenderness angle. If sliding

DOI: 10.1002/eqe

is restricted, a sufficiently slender block/frame uplifts and commences rocking (Figure 2) once the ground acceleration exceeds a minimum magnitude:

$$\ddot{u}_{g,min} = a_{g,min} = g \tan(\alpha) \tag{5}$$

where g is the acceleration of gravity.

When the structure returns to its initial position ($\theta = 0$), impact takes place, the pivot point changes, and the rotation switches sign. A simple way to treat impact is with a coefficient of restitution η, which is taken as the ratio of the pre-impact ($\dot{\theta}^-$) and post-impact ($\dot{\theta}^+$) angular velocities:

$$\dot{\theta}^+ = \eta \dot{\theta}^- \tag{6}$$

The value of the coefficient of restitution is application and material dependent (e.g., [1, 2] and references therein) and, therefore, is considered as an additional, independent, governing parameter of the rocking problem. The results of this study are derived for a coefficient of restitution equal to $\eta = 0.92$. The rocking response is determined numerically solving the nonlinear equations of motion ((4), (5), and (6)) in MATLAB [37].

2.2.2. Engineering demand parameter and limit states (LS). For the purposes of the subsequent fragility analysis (Section 2.3), we need appropriate engineering demand parameters (EDPs) and IMs. According to the assumptions of the present analysis, the former is rather straightforward, because when the rocking structure does not overturn, it eventually returns to its original configuration without permanent deformation or damage. Hence, in accordance with Equation (10) (later on), we adopt as EDP the absolute peak rocking rotation $|\theta_{max}|$ scaled with respect to the slenderness α:

$$EDP = \frac{|\theta_{max}|}{\alpha} \tag{7}$$

The physical meaning of the dimensionless EDP of Equation (7) is clear: Values larger than zero imply that the structure commences rocking, whereas high values (e.g., $EDP > 1.5$) indicate overturning due to rocking. Accordingly, two pertinent performance levels (Table I) assess the vulnerability of a rocking structure (block/frame): *LS1* marks the initiation of rocking, and *LS3* corresponds to overturning due to rocking. In addition, an intermediate limit state *LS2* (Table I) indicates observable rocking during seismic response. The threshold value of *LS2* is based on engineering judgment to express the level of marginal/limited rocking action that is usually targeted in rocking applications. Such limited rocking action, an order of magnitude smaller than the slenderness, seems as a promising balance of the benefits of rocking isolation, without substantial danger of overturning. Table I lists the pertinent EDP values and the qualitative description for each capacity *LS*.

Figures 3 and 4 plot the EDP values ($|\theta_m|/\alpha$) of all nonlinear dynamic response analyses (3500 per structure) versus the peak ground velocity PGV – or V_p in the case of pure pulse ground motions – and the prevailing period T_p of the pulse. Figure 3 concerns a rocking bridge frame/bent [40], with frequency parameter $p = p_f = 1.0$ rad/s and slenderness $\alpha = 0.149$ rad, and Figure 4 a rocking electrical equipment (e.g., [17, 41, 42]) with $p = 2.5$ rad/s and $\alpha = 0.20$ rad. Both structures are subjected to the same two suites of ground motions: One is composed of M&P pulses, and one of CSGMs.

Table I. Proposed performance criteria for rocking behavior.

	EDP ($\|\theta_{max}\|/\alpha$)	Capacity limit states	Description
*LS*1	0.00	Rocking initiation	Uplifting
*LS*2	0.10	Limited rocking	Potential minor and local damage due to contact
*LS*3	$\to \infty$	Rocking overturning	Collapse

EDP, engineering demand parameter; LS, limit states.

DOI: 10.1002/eqe

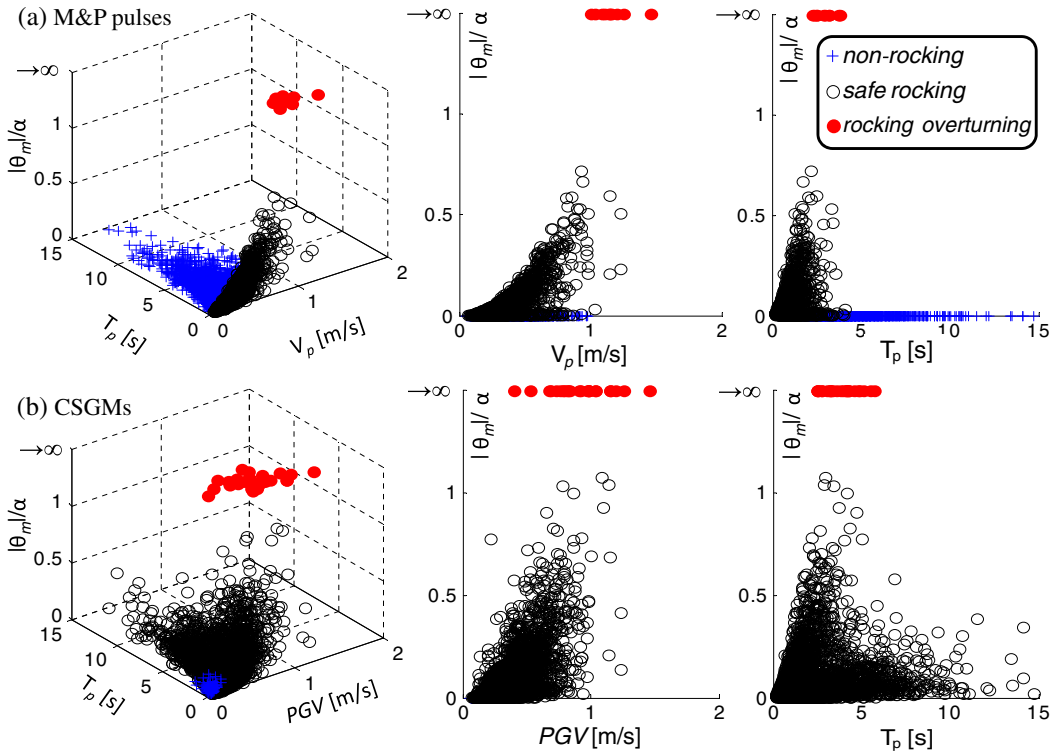

Figure 3. Seismic response analyses of a rocking frame with $p = 1.0$ rad/s and $\alpha = 0.15$ rad.

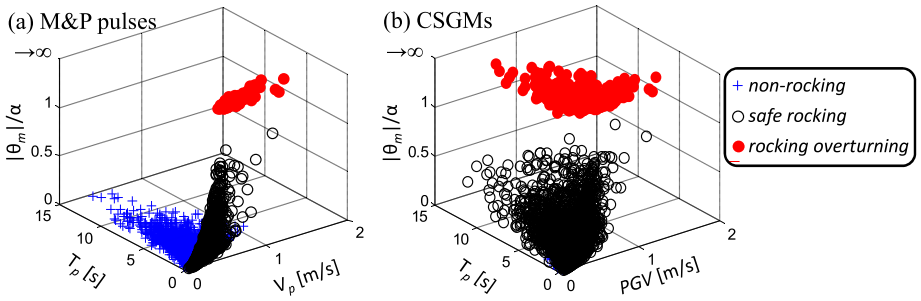

Figure 4. Seismic response analyses of a rocking electrical equipment with $p = 2.5$ rad/s and $\alpha = 0.20$ rad.

Figures 3 and 4 divide the results into three groups: (i) The 'non-rocking' simulations (crosses), when the peak ground acceleration is less than the minimum acceleration that initiates rocking (Equation (5)) and hence the structure remains at rest. (ii) The 'safe-rocking' simulations (hollow circles), when the structure commences rocking and does not overturn/topple, and (iii) the 'rocking-overturning' simulations (solid circles). Recall that a rocking structure becomes statically unstable after $EDP = |\theta_{max}|/\alpha \geq 1.0$, because the highly nonlinear nature of rocking dynamics overturning does not necessarily occur when $EDP \geq 1.0$. On the contrary, a rocking structure might exhibit significantly higher rotations $|\theta_{max}|$ than α without overturning [3], a behavior counter to the common quasi-static viewpoint of seismic response. Overturning occurs, when the system becomes dynamically unstable, in which case the response tends to numerically infinite values. Thus, the threshold of *LS3* does not correspond to a particular rotation value (e.g., $EDP = 1.5$), but rather at $EDP \to \infty$.

Figure 3 bottom panel (Figure 4 right) presents the response when the excitation contains the HFC as described in Section 2.1.3 (CSGM), while Figure 3 top panel (Figure 4, left) when it does not; in which case, the ground motion is a pure M&P pulse as in Section 2.1.1. The low-frequency coherent

DOI: 10.1002/eqe

(M&P) pulses are identical for both rows of Figure 3 (both columns of Figure 4). Thus, Figures 3 and 4 verify the sensitivity of rocking structures to the characteristics of the ground motion (attributed to their negative stiffness) and bring forward the influence of the stochastic HFC in the excitation. Note the apparent straight line on the $V_p - T_p$ plane that separates the 'non-rocking' from the rocking simulations in Figure 3 (top left). The slope of this separating limit line corresponds to the minimum ground acceleration (Equation (5)) that triggers (uplifting and) rocking. However, when the stochastic HFC is present in the excitation, this limit line vanishes (Figure 3, bottom left, and Figure 4, right), the number of 'non-rocking' simulations is drastically reduced, and rocking response becomes significantly more probable. This is because of the numerous CSGMs for which the presence of the HFC triggers rocking, whereas the (low acceleration M&P) pulse alone would not. Consequently, this introduces observable noise in the results (Figure 3, bottom right), and the response becomes less ordered.

Figures 3 and 4 verify also that rocking is sensitive to more than one strong ground motion parameters. Overturning occurs as both PGV and T_p increase, without though a distinguishable pattern. As expected, overturning is more probable for the smaller in size electrical equipment of Figure 4 than the larger rocking frame of Figure 3, the well-known size effect of rocking behavior [15].

2.2.3. Physically similar ('universal') rocking behavior. This section offers a physically consistent, and practically useful, way to scale the rocking behavior for excitations of different intensities and predominant frequencies. With the aid of the proposed scaling, we build (in Section 2.3) normalized fragility curves, indifferent to the size and the frequency of the rocking structure or the amplitude and the predominant frequency of the near-fault ground motion.

Consider a ground motion with a specific waveform (i.e., a specific acceleration time-history shape), for example, the CSGM excitation of Figure 1. Let the (acceleration) amplitude $a_g = PGA$ and the frequency $\omega_g = 2\pi/T_p$ characterize the length and time scale of the waveform, respectively [43]. Then, the response (e.g., the absolute peak rocking rotation $|\theta_{max}|$) can be written as a (usually unknown) function of the general form:

$$|\theta_{max}| = f\left(\alpha, p, \omega_g, \frac{a_g}{g}, \eta\right) \tag{8}$$

Equation (8) contains six characteristic variables that involve only one reference dimension, time $[T]$. The six variables can be grouped into a reduced number of independent dimensionless Π-products according to Buckingham's Π theorem [44]: (6 variables) − (1 reference dimension) = 5Π-products. Specifically,

$$|\theta_{max}| = \phi\left(\frac{\omega_g}{p}, \frac{a_g}{g}, \alpha, \eta\right) \tag{9}$$

where the only dimensionless term arising from dimensional analysis is the frequency ratio ω_g/p. Recall that according to dimensional analysis [45], dimensionless quantities cannot be combined. Hence, the already dimensionless groups of Equation (9) (e.g., the rotation $|\theta_{max}|$ and the angle α) cannot be further combined to reduce the number of the independent dimensionless Π-products.

However, if we distinguish the notion of 'dimension' to that of 'orientation', we can supplement standard dimensional analysis with *orientational analysis* (see, e.g., [2, 46]). In particular, we can demand that the physical equations (e.g., Equations (4) and (9)) are both dimensionally and orientationally homogeneous. Then, the dimensionless groups from Buckingham's theorem (Equation (9)) can be further reduced to dimensionless–orientationless groups [2] as

$$\frac{|\theta_{max}|}{\alpha} = \phi\left(\frac{\omega_g}{p}, \frac{a_g}{g\alpha}, \eta\right) \tag{10}$$

The products/groups of Equation (10) yield an exact representation of the rocking response when the slenderness angle α is small [2]. If α is not small, it should be included explicitly as an additional independent group [2]. For simplicity, let us focus herein on the case of small α (slender rocking structures).

DOI: 10.1002/eqe

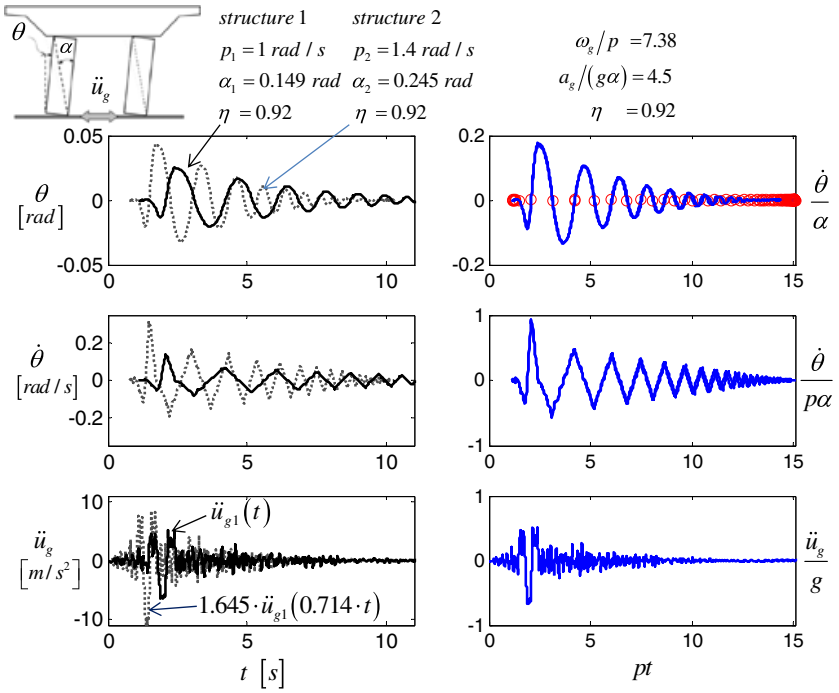

Figure 5. Physically similar rocking response.

Figure 5 demonstrates the merits of adopting the proposed dimensionless–orientationless description of the rocking response: the governing groups of Equation (10). Figure 5 (left) plots the time-history response of two different rocking structures subjected to two (CSGM) excitations of different a_g and ω_g, but the same waveform (of Figure 1). Even though, the two structures differ both in size (p) and in shape (α), when the associated dimensionless–orientationless groups (right-hand side) of Equation (10) take the same values, the response curves of the two different problems collapse into a unique, 'universal' (or 'master') curve (Figure 5). This is a special type of symmetry of unique importance for nonlinear phenomena. It is called *physical similarity* (or *self-similarity* in [45]); the property of physical similarity elucidates what matters in rocking response: the values of the dimensionless governing groups of Equation (10) and not the pertinent dimensional values of, for example, the size (p) or the shape (α) of the structure.

2.3. *Fragility analysis*

In general, fragility (or vulnerability) stands for the conditional probability P_f that an EDP will exceed a certain capacity limit, say c, given an IM value:

$$P_f = P\,(D > C = c \mid IM) \tag{11}$$

More specifically, this study focuses on the conditional probability $P_{f|r}$ that the EDP (Equation (7)) of a structure will exceed a certain (capacity) threshold, given an IM value and given that the structure is rocking. Figure 6 illustrates the probability tree diagram that captures the peculiarities of rocking response and facilitates the calculation of probability $P_{f|r}$. Let P_{nr} denote the probability that the structure will remain resting on the ground (non-rocking response; Figure 6) throughout the earthquake shaking. Recall that rocking only appears if the ground motion acceleration exceeds a minimum threshold (Equation (5)). Let also P_{ro} denote the probability that rocking occurs and results in overturning. Then, the probability $P_{f|r}$ that the EDP will exceed a certain capacity limit given an IM value is derived by the union of two likelihoods (Figure 6): (a) Rocking results in

DOI: 10.1002/eqe

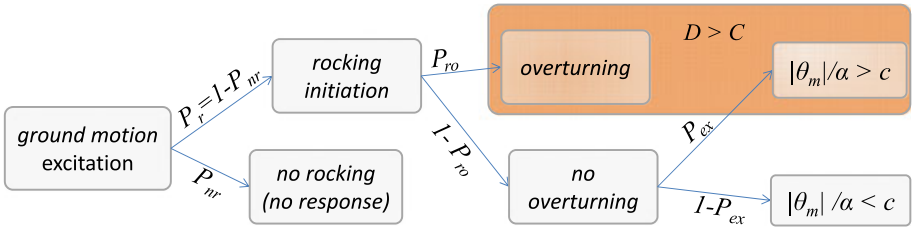

Figure 6. Probability tree diagram for the rocking problem.

overturning, and (b) the structure survives the excitation, but during its rocking response, the EDP exceeds the capacity limit c. Thus, Equation (11) becomes [31]

$$P_{f|r} = P_{ro} + (1 - P_{ro})\, P_{ex}\,(D > C \mid IM) \tag{12}$$

Sections 2.3.1 to 2.3.3 zoom in Equation (12) and explain how each term can be calculated.

2.3.1. Intensity measures. A far from trivial, the longstanding challenge (e.g., [10]) is to identify appropriate IM/s for rocking structures. A rational approach is to select IMs that 'mimic' the proposed dimensionless–orientationless groups of Equation (10), and instead of dimensional IMs to use dimensionless IMs similar to that in [41] for sliding objects. Referring again to Equation (10), there are two groups that could be considered as candidate IMs: the frequency ratio ω_g / p and the dimensionless slenderness $a_g/(g \tan\alpha)$. The former hinges on a time scale of the excitation ω_g, while the latter on a length scale of the excitation a_g. We examine four common strong ground motion parameters that could be used as a_g or ω_g accordingly: the peak ground velocity PGV ($= V_p$ for pulse excitations), the peak ground acceleration PGA, the predominant period T_p of the pulse, and the mean period of the CSGM T_m (see [43] and references therein). Using the four well-known strong ground motion parameters, we construct the following alternative versions of the two groups ω_g / p and $a_g/(g \tan\alpha)$:

$$IM_1 = \frac{\omega_p}{p},\ IM_2 = \frac{\omega_m}{p},\ IM_3 = \frac{PGA}{pPGV},\ IM_4 = \frac{PGA}{g\tan\alpha},\ IM_5 = \frac{pPGV}{g\tan\alpha},\ IM_6 = \frac{\omega_m PGV}{g\tan\alpha} \tag{13}$$

where $\omega_p = 2\pi/T_p$, $\omega_m = 2\pi/T_m$, p is the rocking frequency parameter of the structure, α is the slenderness angle, and g is the acceleration of gravity. IMs IM_1 to IM_3 (Equation (13)) reconstruct the frequency ratio (ω_g / p; Equation (10)), whereas IM_4 to IM_6 (Equation (13)) are alternative dimensionless slenderness ($a_g/(g\tan\alpha)$; Equation (10)) groups. In the following, we refer to the former as '*frequency ratio*' IMs and to the latter as '*dimensionless slenderness*' IMs.

In Section 2.3.2, we examine first the most appropriate and/or proficient [47] IMs in terms of their ability to reduce the dispersion in the (response) results. Then, we illustrate the superiority of bivariate IMs over univariate IMs and proceed accordingly with their selection.

2.3.2. Probability of limit state exceedance during 'safe' rocking. This section focuses on the calculation of the conditional probability P_{ex} (Figure 6 and Equation (12)) that a ground motion with $IM = x$ will cause the exceedance of a performance/capacity limit c, without the occurrence of overturning ('safe rocking').

The calculation procedure is based on two typical assumptions. Firstly, that both the capacity C and the demand D are random variables following lognormal distributions. Then, P_{ex} can be written as follows:

$$P_{ex} = P_{ex}\,(D > C \mid IM = x) = \Phi\left(\frac{\ln x - \mu}{\beta_{D|IM}}\right) \tag{14}$$

DOI: 10.1002/eqe

where $\Phi()$ is the *standard* (i.e., with mean 0 and standard deviation 1) normal cumulative distribution function, x are the values of the EDP, μ is the median value of the structural demand as a function of IM, and $\beta_{D|IM}$ is the dispersion, or logarithmic standard deviation, of the demand conditioned on the IM [47].

The second typical assumption (Cornell *et al.*[48]) is that the median demand D_m and the IM obeys a scale law, such that

$$D_m = a\,(IM)^b \tag{15}$$

Conveniently, the assumed scale law (Equation (15)) becomes a straight line on the $\ln D_m$ *vs* $\ln IM$ plane:

$$\ln(D_m) = \ln(a) + b\ln(IM) \tag{16}$$

which enables the estimation of parameters a and b by means of linear regression analysis.

Figure 7 presents sample results of the linear regression analyses considering solely the 'safe-rocking' cases (of Figure 3). Again, Figure 7(a) concerns pure pulse excitations (Section 2.1.1), whereas part Figure 7(b) adds on the same pulses the stochastic HFC (generating CSGMs according to Section 2.1.3). Figure 8 offers a comparative evaluation of all candidate *IM*s of Equation (13). The performance of the IMs is assessed with respect to their ability to reduce the dispersion of the response

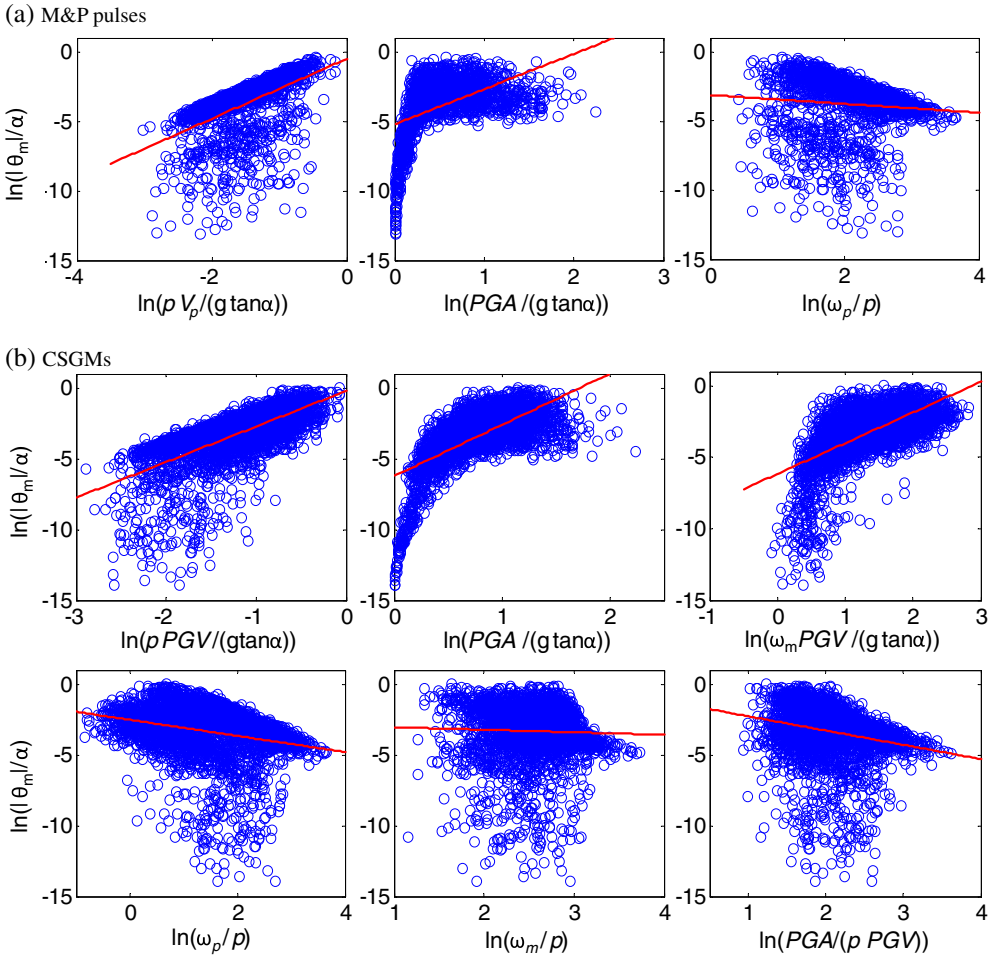

Figure 7. Sample results of the linear-regression analyses for (a) pure M&P pulse excitations and (b) CSGMs. None of the examined IMs exhibits a strong effect on the response.

DOI: 10.1002/eqe

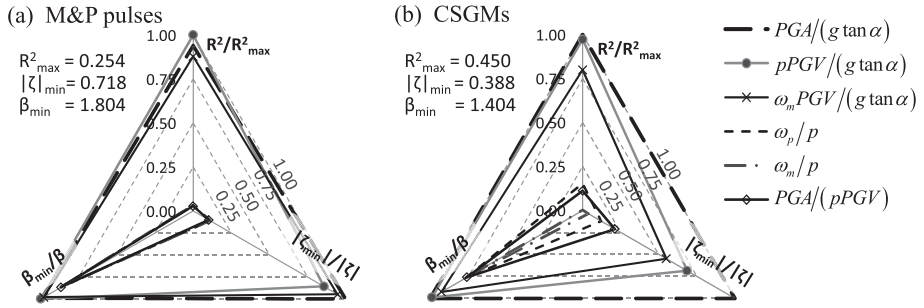

Figure 8. Comparative evaluation of the candidate IMs of Equation (14) in terms of three dispersion measures: R^2, $\beta_{D|IM}$, and ζ. If an IM encloses the others, it performs better.

(results). As measures of dispersion, we consider the coefficient of determination R^2, the logarithmic standard deviation $\beta = \beta_{D|IM}$, and the proficiency $\zeta = \beta_{D|IM}/b$ proposed by Padgett *et al.* [47]. R_{max}, β_{min}, and $|\zeta_{min}|$ (in Figure 8) are the pertinent maximum and minimum values, accordingly, among all examined IMs.

The best IMs are (Figure 8) the ones expressing the dimensionless slenderness $(a_g/(g\tan\alpha))$, and primarily $IM_4 = PGA/(g\tan\alpha)$ and $IM_5 = (pPGV)/(g\tan\alpha)$. Note that for a particular structure (given p, α values), the performance of IM_4 and IM_5 is determined solely by PGA and PGV, respectively (two traditional IMs in earthquake engineering). On the contrary, IM_6 hinges on both a time scale T_m and a length scale PGV of the excitation. The dimensionless slenderness IMs (IM_4 to IM_6) present small differences for M&P pulses, but $IM_4 = PGA/(g\tan\alpha)$ is the most *proficient* [47] for CSGMs. Among the examined frequency ratio IMs (IM_1 to IM_3 in Equation (13)), the most *proficient* is $IM_3 = PGA/(pPGV)$, again, for the more challenging case of CSGMs (Figure 8(b)). In general though, the performance of all examined frequency ratio IMs is surprisingly poor. Recall that, on the contrary, rocking response to (trigonometric) pulse excitations is very sensitive to the ω_p/p ratio and becomes more ordered for higher ω_p/p values [2]. Still, even for pure M&P pulse ground motions (Figure 8(a)), none of the frequency ratio IMs achieves a strong correlation with the response.

Importantly, Figure 7 unveils a lack of a distinguishable linear trend in the response. In other words, regardless which of the IMs performs best compared with the others, none of the examined IMs shows a strong effect on the response. Partly, this failure of traditional strong ground motion parameters (e.g., PGA, PGV, and PGA/PGV) to capture rocking response should be attributed to the negative stiffness mechanism and subsequently the lack of resonance of rocking structures under constant frequency ground motions; for example, [11]. At this point, recall in [49] that an *IM* might affect the structural response very differently if considered individually, as opposed to when it is combined with a second *IM*. For instance, when either the length scale a_g or the time scale ω_g of an excitation is considered separately as the single IM, the analysis overlooks the strong dependency of the structural behavior on the other IMs. This simple observation motivates a different, more 'holistic', approach of the problem.

Figure 9 (left and right) presents a three-dimensional view, $\ln(|\theta_m|/\alpha) - \ln V_p - \ln T_p$, of the same 'safe-rocking' simulations (of Figure 3) as Figure 7(a) and (b), respectively. If viewed from the proper viewpoint (Figure 9), remarkable order emerges: The response points lie consistently on two distinct planes; a trend is completely hidden in the two-dimensional representations of the same results (e.g., Figure 7). The existence of the two distinct planes unveils that rocking response scales differently for low intensity, versus high intensity, excitations. Put simply, rocking is more sensitive to low amplitude excitations, in the sense that even slight variations of the excitation characteristics have a dramatic effect on the peak rocking response. Both 'low' (e.g., $PGA < 1.30a_{g,min}$) and 'high' (e.g., $PGA > 1.30a_{g,min}$) amplitudes are defined according to the minimum rocking acceleration $a_{g,min} = g\tan\alpha$, a characteristic property of the structure. For economy of space, we omit the presentation of the best fits with more conventional distributions: linear (planar), bilinear, or higher-order two-dimensional distributions, because they result in inferior approximations compared with the proposed biplanar distribution of Figure 9. The recent study of Acikgoz and DeJong [10] marked a region, with

DOI: 10.1002/eqe

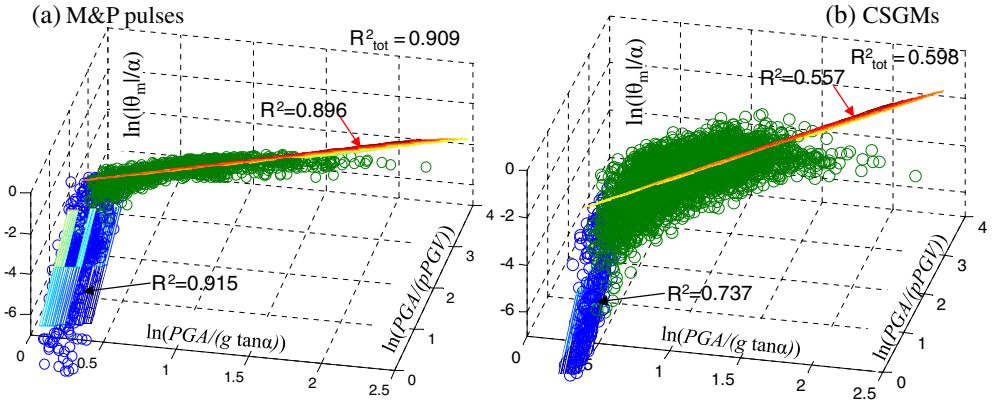

Figure 9. Three-dimensional illustration of the same 'safe-rocking' results as Figure 7. The proper viewpoint unveils remarkable order: the response points, for M&P pulse excitations (a) and for the combined synthetic ground motions (b), lie consistently on two distinct planes.

Table II. The fitted biplanar distributions $a\left(\frac{PGA}{g\tan\alpha}\right)^{b_1}\left(\frac{PGA}{pPGV}\right)^{b_2}$ for the response analyses of Figures 3 and 4.

Excitation	Structure ($p\alpha$)	$1.00 < PGA/(g\tan\alpha) < 1.30$				$PGA/(g\tan\alpha) \geq 1.30$			
	(rad/s | rad)	a	b_1	b_2	(R^2)	a	b_1	b_2	(R^2)
M&Ps	frame (1.0|0.15)	0.001	29.40	−1.994	(0.915)	1.490	1.574	−2.004	(0.896)
M&Ps	el.eq. (2.5|0.19)	0.001	30.51	−2.027	(0.883)	1.484	1.644	−2.013	(0.872)
CSGMs	frame (1.0|0.15)	6.02e-6	28.31	−0.236	(0.737)	0.104	2.640	−1.436	(0.557)
CSGMs	el.eq. (2.5|0.19)	11.3e-6	30.39	−0.072	(0.724)	0.063	2.954	−0.942	(0.370)

M&P, Mavroeidis and Papageorgiou; CSGM, combined synthetic ground motion.

almost the same boundaries, as sensitive to uplift because of the HFC. To the best of our knowledge though, this is the first time a clear response pattern is detected and quantified (Table II).

Importantly, the generic equation of a plane in a three-dimensional ($\ln(|\theta_m|/\alpha) - \ln IM_x - \ln IM_y$) space is as follows:

$$\ln(D_m) = b_1 \ln(IM_x) + b_2 \ln(IM_y) + \ln(a) \tag{17}$$

which implies that the mean demand is given by a bivariate (vector-valued) intensity measure $I\hat{M} = \left(IM_x, IM_y\right)$ as

$$D_m = a\left(IM_x^{b_1} IM_y^{b_2}\right) \tag{18}$$

where IM_x and IM_y are two appropriate (scalar) IMs, and a, b_1, b_2 are coefficients calculated using multi-linear regression analysis [50]. For IM_x and IM_y, we adopt the best dimensionless slenderness IM ($IM_4 = PGA/(g\tan\alpha)$) and the best frequency ratio IM ($IM_3 = PGA/(pPGV)$) of Figure 8, respectively. Figure 8 is not directly applicable to the biplanar distribution; however, the results of the analysis indicate that it still offers a representative ranking of the relative performance of the examined IMs.

The transition between the two planes takes place at a constant acceleration boundary (Figure 9). Iterative multi-linear regression analyses allow the location of the transition limit through the minimization of the dispersion (e.g., the coefficients of determination R^2) of both planes of Figure 9 simultaneously. Approximately, this happens for $PGA/(g\tan\alpha) = 1.30$. Table II lists the regression parameters a, b_1, b_2 and the coefficient of correlation R^2 for the fitted biplanar distributions.

DOI: 10.1002/eqe

Consider again the two different structures: the rocking frame from Figure 3 and the rocking electrical equipment (el.eq.) from Figure 4. Table II gives the fitted biplanar distributions when these structures are subjected to the same suite of ground motions, either pure (M&P) pulses or CSGMs. The agreement of the biplanar distributions, for the two different structures (different p and α values), verifies the 'universal' character of the observed pattern. The agreement is excellent for pure M&P excitations (Table II), for which, in addition, the R^2 values disclose an almost deterministic behavior (Figure 9). Note that the coefficient of determination values for the whole range of the biplanar distributions (not shown in Table II) are as follows: $R^2 = 0.909$ (0.881) under M&P pulse excitations and $R^2 = 0.598$ (0.568) under CSGMs, for the rocking frame (electrical equipment), respectively. Not surprisingly, the agreement is not as satisfying for CSGMs, as characterizing a complex waveform (like the CSGMs) with solely two numbers—two common strong ground motion parameters, for example, $a_g = PGA$, $\omega_g = 2\pi/T_p$—results in loss of information. For instance, the analysis herein neglects the effect of the duration of the excitation on rocking response [11]. Clearly, this is a limitation of the proposed approach and an open issue for further research towards new, improved IMs tailored to the needs of rocking structures. However, this task goes beyond the scope of the present paper. Further, the presence of the HFC adds, as expected, noise in the response (Figure 9, right) that is reflected in the lower R^2 values. Still, the proposed biplanar distribution succeeds not only in reducing the overall dispersion but also in bringing forward the existence of a strong—and, to date, unknown – response pattern.

Finally, Figure 10 plots the probability of *LS2* (Table I) exceedance P_{ex} fragility curves for the best scalar IM (Equation (15)) and for the vector-valued IM of Equation (18), adopting the common lognormal assumption (Equation (14)). The superiority of the bivariate fragility curves (FCs) becomes apparent when compared with conventional FCs for given PGA/PGV values. For example, Figure 10 compares univariate with bivariate FCs for given PGA/PGV values. As the PGA/PGV ratio increases, the fragility of the rocking structure (Figure 10) decreases, a well-known trait of rocking behavior that the univariate FC neglects. In addition, the univariate FC is flatter than the bivariate FCs, which indicates higher uncertainty.

2.3.3. Probability of collapse. The likelihood of overturning due to rocking (with probability P_{ro} in Figure 6), as well as of non-rocking (with probability P_{nr}), is expressed with a '*categorical*' [50] response variable. In particular, a zero-valued (0) or one-valued (1) parameter suffices to describe overturning (or rocking initiation), because the structure either overturns or not (similarly, the structure either commences rocking or not). In both cases, the 'categorical' nature of the response hinders the calculation of the statistical moments (mean μ and standard deviation β) necessary for estimating the probability as (e.g.) in Section 2.3.2.

The numerical results of the response analyses could provide a posterior estimation (e.g., [31]) of P_{nr} = (*number of non-rocking simulations*)/(*total number of simulations*) and P_{ro} = (*number of rocking-overturning simulations*)/(*total number of rocking simulations*). Nevertheless, to derive a predictive (a priori) expression for the probability $P_{f|r}$, we need to calculate $P_{f|r}$, and subsequently P_{nr} and P_{ro} (Equation (12)), as a function of the adopted IM/s. In lieu of the method of moments, we employ a *maximum likelihood estimation* (MLE) approach (see, e.g., [26, 49, 51]) and

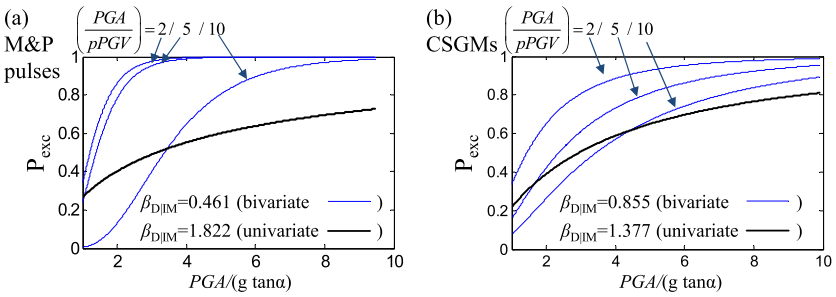

Figure 10. Comparison of bivariate with univariate P_{ex} fragility curves for different $pPGV/PGA$ values.

DOI: 10.1002/eqe

calculate the fragility function parameters (e.g., μ and β in Equation (20)) for which the assumed statistical distribution attains the highest likelihood of producing the observed data. The likelihood function L is as follows:

$$L = \prod_{j=1}^{n} P_{ro}^{z_j} \, (1 - P_{ro})^{1-z_j} \tag{19}$$

where z_j is the *binomial distribution* [50] variable, equal to unity when overturning occurs and null otherwise. P_{ro} is the probability of (rocking) overturning, for which again the common, but not unique (e.g., Gehl *et al.*[49]), assumption is given by a lognormal cumulative distribution function. The probability P_{ro} that a ground motion with $IM = x$ will cause overturning then becomes

$$P_{ro} = P_{ro}\,(D \geq overturn. \mid IM = x) = \Phi\left(\frac{lnx - \mu}{\beta}\right) = \frac{1}{2}\left(1 + erf\left(\frac{\ln x - \mu}{\beta\sqrt{2}}\right)\right) \tag{20}$$

where *erf* is the error function. Substituting Equation (20) into Equation (19), the likelihood function L takes the following form:

$$L = \prod_{j=1}^{n} \Phi\left(\frac{lnx_j - \mu}{\beta}\right)^{z_j} \left(1 - \Phi\left(\frac{lnx_j - \mu}{\beta}\right)\right)^{1-z_j} \tag{21}$$

Numerical optimization [37, 51] returns the parameters $\hat{\mu}, \hat{\beta}$ that maximize L:

$$\left\{\hat{\mu}, \hat{\beta}\right\} = \max_{\mu,\beta} \prod_{j=1}^{n} \Phi\left(\frac{\ln x_j - \mu}{\beta}\right)^{z_j} \left(1 - \Phi\left(\frac{\ln x_j - \mu}{\beta}\right)\right)^{1-z_j} \tag{22}$$

In a similar way (with Equations (19) to (22)), one could estimate the probability of non-rocking P_{nr} or, in other words, the probability of *LS1* exceedance (Table I). An additional benefit of adopting a PGA-based dimensionless slenderness IM (e.g., $IM_4 = PGA/(g\tan\alpha)$) though is that such a calculation is not necessary, as rocking initiation becomes—at least in theory—deterministic. Ground motions with $PGA \geq (g\tan\alpha)$ trigger rocking (hence $P_{nr} = 0$), whereas ground motions with $PGA < (g\tan\alpha)$ do not (in which case $P_{nr} = 1$). Therefore, we omit the calculation of P_{nr}.

The examined rocking frame ($p = 1.0$ rad/s and $\alpha = 0.15$ rad) rarely overturns (Figure 3). Thus, its response does not offer enough observation/data to estimate, in an unbiased and efficient manner, the probability of overturning with the MLE procedure. For this reason, the present section focuses on the response of the electrical equipment of Figure 4. Figure 11 plots the P_{ro} (probability of overturning) fragility curves as calculated with the aid of the MLE method for different *IM*s. If the P_{ro} fragility curves of Figure 11 were based on the limited rocking frame data, the μ and β values would be $\mu = 0.762$ (0.870) and $\beta = 0.113$ (0.155) under M&P pulses (and under CSGMs accordingly). Figure 11 depicts also the numerical simulation results (data) with circles of different areas. The ordinate (y-coordinate) of each circle is the percentage of collapse occurrences within the specific IM value (strip). For instance, an ordinate of 0.4 means that 40% of the analyses for that particular IM value (strip) resulted in overturning. The size of the circle indicates the number of the pertinent data (the wider the circle, the more the corresponding observations).

Interestingly, a pure M&P pulse excitation with the same PGV as a CSGM leads to higher probability of overturning and lower dispersion, that is, to more conservative results (Figure 11). This observation seems to corroborate the extensive use of pure pulse ground motions in literature (e.g., [2, 3, 16–19]) as a means of elucidating the overturning trends of a rocking structure. Recall though that the absolute number of overturning occurrences is significantly smaller for M&P pulses, compared with CSGMs (Section 2.2.2). In other words, if the pulse is capable of initiating rocking, it is more likely to cause overturning than a CSGM excitation of the same PGV. Further, unlike the fragility in the case of 'safe rocking' (Section 2.3.2), $pPGV/(g\tan\alpha)$ outperforms, for example, in terms of standard deviation β, all other scalar IMs. On the contrary, the performance of $PGA/(g\tan\alpha)$ is remarkably poor,

DOI: 10.1002/eqe

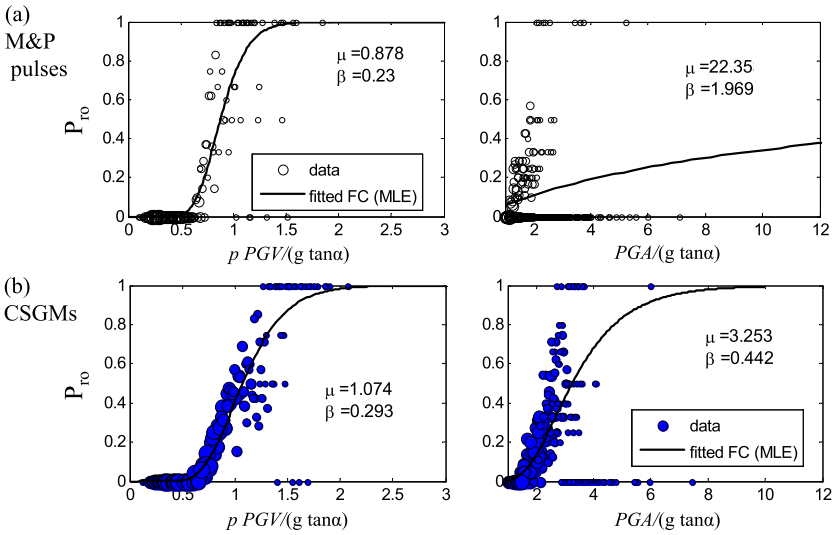

Figure 11. Rocking overturning fragility curves (P_{ro}) for different types of excitations and different univariate (dimensionless) IMs.

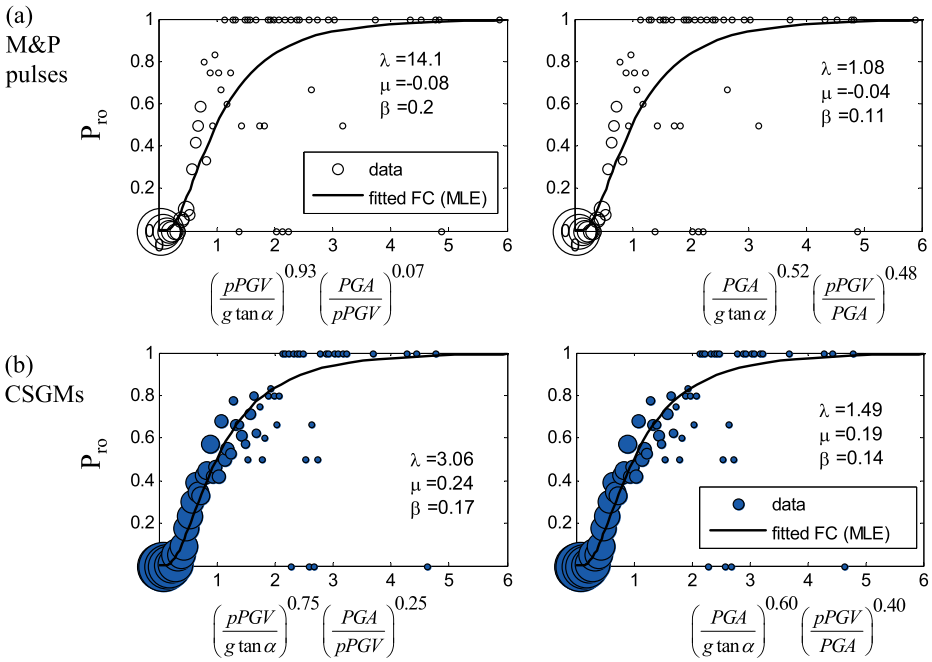

Figure 12. Rocking overturning fragility curves (P_{ro}) for different types of excitations and different bivariate, hybrid (dimensionless) IMs.

especially for pure pulses (Figure 11, top right). Yet, as Figures 11 and 12 illustrate later on, rocking overturning is primarily a matter of velocity. Recall (e.g., [2]) that critical overturning conditions for a rocking block can be derived from velocity criteria, usually the angular velocity of the structure at the time instant the excitation ends. A PGA-based IM alone (e.g., $IM_4 = PGA/(g\tan\alpha)$) cannot capture response velocity and, hence, fails to correlate strongly with overturning.

Therefore, as a more refined approach, we employ a linear combination of two IMs and seek a hybrid, bivariate, intensity measure $I\hat{M}$ of the following form:

DOI: 10.1002/eqe

$$\ln(I\hat{M}) = \frac{\lambda}{1+\lambda} lnIM_x + \frac{1}{1+\lambda} lnIM_y \tag{23}$$

similar to that in [49] (for a different type of structures). We employ a dimensionless slenderness IM as IM_x and supplement it with a frequency ratio IM for IM_y. At the two λ extremes, we retrieve one of the two scalar IM components. Specifically, for $\lambda = 0$, Equation (23) gives $\ln(I\hat{M}_i) = \ln(IM_y)$, while for $\lambda \to \infty$: $\ln(I\hat{M}_i) = \ln(IM_x)$. Instead of Equation (20), probability P_{ro} now becomes a bivariate function of argument $I\hat{M}(IM_1, IM_2) = x(IM_1, IM_2) = x$ equal with

$$P_{ro}\left(D \geq overturn. \mid x\left(IM_1, IM_2\right)\right) = \frac{1}{2}\left(1 + erf\left(\frac{1}{\beta\sqrt{2}}\left(\frac{\lambda}{1+\lambda} lnIM_1 + \frac{1}{1+\lambda} lnIM_2 - \mu\right)\right)\right) \tag{24}$$

where erf is the error function, μ is the mean value, and β is the standard deviation. Note that the IM of Equation (18) is a special case of that of Equation (23), because the two IMs are equivalent when

$$a = 1,\ b_1 = \frac{\lambda}{1+\lambda},\ b_2 = \frac{1}{1+\lambda} \tag{25}$$

Figure 12 plots the overturning fragility curves (P_{ro}) as calculated with the MLE method. Similar to Figure 11, Figure 12 compares two dimensionless slenderness IMs, $PGA/(g\tan\alpha)$ and $pPGV/(g\tan\alpha)$, using, for economy of space, only the most efficient frequency ratio IM: $pPGV/PGA$. In general, the use of hybrid, bivariate $I\hat{M}$s reduces the dispersion (standard deviation β) compared with the pertinent scalar IMs (Figure 11). Complementing a PGA-based IM $PGA/(g\tan\alpha)$ with a frequency ratio IM yields a hybrid, bivariate IM, at least as efficient as the univariate $pPGV/(g\tan\alpha)$. This is true for both types of excitations: M&P pulses and CSGMs.

3. PROPOSED 'UNIVERSAL' FRAGILITY CURVES

Sections 2.3.2 and 2.3.3 offer the probability of a limit state threshold being exceeded during 'safe rocking' P_{ex} and the probability of rocking overturning P_{ro}, respectively. With these two key ingredients (P_{ex} and P_{ro}) at hand, the calculation of the seismic rocking fragility $P_{f|r}$ becomes simple for any desired limit state threshold (Equation (12) and Figure 6). For the calculation, one can use either a univariate or a bivariate IM. An efficient univariate IM to capture both rocking overturning (i.e., P_{ro}) and 'safe-rocking' response (i.e., P_{ex}) is $pPGV/(g\tan\alpha)$ in accordance with [10]. On the other hand, the pair of IMs, ($PGA/(g\tan\alpha)$, $pPGV/PGA$), forms a bivariate IM powerful in predicting both P_{ro} and P_{ex}, simply by altering the exponents. While, the use of a univariate IM is a simpler approach, it results in increased scatter. On the other hand, the more complex bivariate IM approach reduces drastically the uncertainty, but at the cost of additional information about the frequency content of the ground motion.

In either case, the study proposes the use of dimensionless IMs, by scaling strong ground motion parameters with respect to the dynamic characteristics of the structure. In this way, a 'universal' description of rocking fragility is achieved for pure pulse ground motion and an approximately 'universal' description for CSGMs (Section 2.2.3 and Table II). It follows that for a given ground motion, two different structures (different p and α values) yield different IM values, reflecting their corresponding seismic fragility. For instance, consider a CSGM with $PGA = 0.5g$ and $PGA/PGV = 2$. Then, according to the bivariate FC of Figure 12 (bottom right), the probability of overturning of a rocking frame (with $p = 1.0$ rad/s and $\alpha = 0.15$ rad) is $P_{ro}(1.55) = 0.73$, whereas the probability of overturning of a rocking electrical equipment (with $p = 2.5$ rad/s and $\alpha = 0.20$ rad) is $P_{ro}(1.88) = 0.81$. Recall that the P_{ro} calculations for both structures are based on the response of the electrical equipment, as the rocking frame does not overturn often enough to yield reliable FCs. For CSGMs, this introduces a small error, as the proposed normalized fragility estimation is (for CSGMs) only approximately 'universal'. This is obvious for example also in the differentiation of the biplanar distributions between M&Ps and CSGMs in Table II. Still, the increased

DOI: 10.1002/eqe

probability of overturning of the smaller (higher frequency parameter p) structure verifies the well-known size effect of rocking behavior [15]: The larger the structure, the more safe it is against rocking overturning.

As a future extension, the proposed herein fragility curves could be used to estimate the fragility of a large class of very different rocking structures (e.g., the rocking wall, the rocking arch, or the asymmetric rocking frame) via the recently proposed methodology in [1]. Recall that the DeJong and Dimitrakopoulos [1] study yields the essential rocking parameters required to derive dynamic equivalence with the rocking block. The equivalence is exact for single-block rocking mechanisms and (usually, but not always) approximate for multi-block rocking structures.

4. CONCLUSIONS

This paper offers analytical FCs for slender, rigid structures rocking under (synthetic) near-fault ground motions. The FCs are either univariate (conventional) or bivariate, based accordingly on a univariate or bivariate IM/s. The study shows that when information about the frequency content of the excitation is available, the bivariate FCs offer a superior estimation of the fragility, compared with the conventional univariate FCs. Further, the paper also unveils that when the rocking structure survives the excitation without overturning, the peak response follows a biplanar distribution. In this context, it brings forward the existence of a critical peak ground acceleration, below and above which, rocking response scales differently. The results, especially for pure pulse ground motions, show remarkable order in the rocking response.

In pursuit of an efficient description of fragility, the study resorts to dimensionless–orientationless IMs. The proposed IMs offer a normalized (approximately 'universal') description of rocking, indifferent to the size and frequency of the structure or the amplitude and predominant frequency of the (near-fault) ground motion. Thus, for a given ground motion, different structures yield different IM values, reflecting their corresponding seismic fragility. In this context, the analysis also reveals the need for new, improved, specialized IMs tailored to the peculiarities of rocking behavior.

ACKNOWLEDGMENTS

Financial support was provided by the Research Grants Council of Hong Kong, under grant reference number ECS 639613.

REFERENCES

1. DeJong MJ, Dimitrakopoulos EG. Dynamically equivalent rocking structures. *Earthquake Engineering & Structural Dynamics* 2014. (in press) DOI: 10.1002/eqe.2410.
2. Dimitrakopoulos EG, DeJong MJ. Revisiting the rocking block: closed-form solutions and similarity laws. *Proceedings of the Royal Society A: Mathematical, Physical and Engineering Science* 2012; **468**(2144): 2294–2318.
3. Dimitrakopoulos EG, DeJong MJ. Overturning of retrofitted rocking structures under pulse-type excitations. *Journal of Engineering Mechanics* 2012; **138**(8):963–972.
4. Papaloizou L, Komodromos P. Planar investigation of the seismic response of ancient columns and colonnades with epistyles using a custom-made software. *Soil Dynamics and Earthquake Engineering* 2009; **29**(11):1437–1454.
5. Papaloizou L, Komodromos P. Investigating the seismic response of ancient multi-drum colonnades with two rows of columns using an object-oriented designed software. *Advances in Engineering Software* 2012; **44**(1):136–149.
6. Beck JL, Skinner RI. The seismic response of a reinforced concrete bridge pier designed to step. *Earthquake Engineering and Structural Dynamics* 1974; **2**(4):343–358. DOI: 10.1002/eqe.4290020405.
7. Kelly JM, Tsztoo DF. Earthquake simulation testing of a stepping frame with energy-absorbing devices. *Bulletin of the New Zealand National Society for Earthquake Engineering* 1977; **10**(4):196–207.
8. Antonellis G, Panagiotou M. Seismic response of bridges with rocking foundations compared to fixed-base bridges at a near-fault site. *Journal of Bridge Engineering* 2013; **19**(5).
9. Makris N, Konstantinidis D. The rocking spectrum and the limitations of practical design methodologies. *Earthquake Engineering and Structural Dynamics* 2003; **32**(2):265–289.
10. Acikgoz S, DeJong MJ. The rocking response of large flexible structures to earthquakes. *Bulletin of Earthquake Engineering* 2014; **12**(20):875–908.
11. DeJong MJ. Amplification of rocking due to horizontal ground motion. *Earthquake Spectra* 2012; **28**(4):1405–1421.

12. Spanos PolD, Koh AS. Rocking of rigid blocks due to harmonic shaking. *Journal of Engineering Mechanics* 1984; **110**(11):1627–1642.
13. Hogan SJ. On the dynamics of rigid-block motion under harmonic forcing. *Proceedings of the Royal Society of London. A. Mathematical and Physical Sciences* 1989; **425**(1869):441–476.
14. Lenci S, Rega G. A dynamical systems approach to the overturning of rocking blocks. *Chaos, Solitons & Fractals* 2006; **28**(920):527–542.
15. Housner GW. The behavior of inverted pendulum structures during earthquakes. *Bulletin of the Seismological Society of America* 1963; **53**(2):403–417.
16. Anooshehpoor A, Heaton TH, Shi B, Brune JN. Estimates of the ground accelerations at point Reyes station during the 1906 San Francisco earthquake. *Bulletin of the Seismological Society of America* 1999; **89**(4):845–853.
17. Zhang J, Makris N. Rocking response of free-standing blocks under cycloidal pulses. *Journal of Engineering Mechanics* 2001; **127**(5):473–483.
18. Voyagaki E, Psycharis IN, Mylonakis G. Rocking response and overturning criteria for free standing rigid blocks to single-lobe pulses. *Soil Dynamics and Earthquake Engineering* 2013; **46**:85–95.
19. Voyagaki E, Psycharis IN, Mylonakis G. Journal of Engineering Mechanics 2013; **140**(6).
20. Aydin K, Tung CC. Energy balance equation for estimating overturning potential of an unanchored rocking body subjected to earthquake excitation. *Earthquake Spectra* 2001; **17**(2):209–220.
21. Yim CS, Chopra AK, Penzien J. Rocking response of rigid blocks to earthquakes. *Earthquake Engineering & Structural Dynamics* 1980; **8**(6):565–587.
22. Spanos PolD, Koh AS. Analysis of block random rocking. *Soil Dynamics and Earthquake Engineering* 1986; **5**(3):178–183.
23. Cai GQ, Yu JS, Lin YK. Toppling of rigid block under evolutionary random base excitations. *Journal of Engineering Mechanics* 1995; **121**(8):924–929.
24. Shao Y, Tung C. Seismic response of unanchored bodies. *Earthquake Spectra* 1999; **15**(3):523–536.
25. ATC. *Seismic vulnerability and impact of disruption of lifelines in the conterminous US*, 1991. Redwood City, CA, Applied Technology Council.
26. Shinozuka M, Feng MQ, Lee J, Naganuma T. Statistical analysis of fragility curves. *Journal of Engineering Mechanics* 2000; **126**(12):1224–1231.
27. Kafle B, Nelson L, Gad EF, Wilson J. Displacement controlled rocking behaviour of rigid objects. *Earthquake Engineering and Structural Dynamics* 2011; **40**(15):1653–1669.
28. Roh H, Cimellaro GP. Seismic fragility evaluation of RC frame structures retrofitted with controlled concrete rocking column and damping technique. *Journal of Earthquake Engineering* 2011; **15**(7):1069–1082.
29. Deng L, Kutter BL, Kunnath SK. Probabilistic seismic performance of rocking-foundation and hinging-column bridges. *Earthquake Spectra* 2012; **28**(4):1423–1446.
30. Roh H, Reinhorn AM. Nonlinear static analysis of structures with rocking columns. *Journal of Structural Engineering* 2009; **136**(5):532–542.
31. Psycharis IN, Fragiadakis M, Stefanou I. Seismic reliability assessment of classical columns subjected to near-fault ground motions. *Earthquake Engineering & Structural Dynamics* 2013; **42**(14):2061–2079.
32. Taflanidis AA. Optimal probabilistic design of seismic dampers for the protection of isolated bridges against near-fault seismic excitations. *Engineering Structures* 2011; **33**(12):3496–3508.
33. Lamprou A, Jia G, Taflanidis AA. Life-cycle seismic loss estimation and global sensitivity analysis based on stochastic ground motion modeling. *Engineering Structures* 2013; **54**:192–206.
34. Boore DM. Simulation of ground motion using the stochastic method. *Pure and Applied Geophysics* 2003; **160** (3-4):635–676.
35. Mavroeidis GP, Papageorgiou AS. A mathematical representation of near-fault ground motions. *Bulletin of the Seismological Society of America* 2003; **93**(3):1099–1131.
36. Rupakhety R, Sigurdsson SU, Papageorgiou AS, Sigbjrnsson R. Quantification of ground-motion parameters and response spectra in the near-fault region. *Bulletin of Earthquake Engineering* 2011; **9**(4):893–930.
37. Natick MA. MATLAB, Mathworks. 2012.
38. Halldórsson B, Mavroeidis GP, Papageorgiou AS. Near-fault and far-field strong ground-motion simulation for earthquake engineering applications using the specific barrier model. *Journal of Structural Engineering* 2010; **137**(3):433–444.
39. Atkinson GM, Silva W. Stochastic modeling of California ground motions. *Bulletin of the Seismological Society of America* 2000; **90**(2):255–274.
40. Makris N, Vassiliou MF. Planar rocking response and stability analysis of an array of free-standing columns capped with a freely supported rigid beam. *Earthquake Engineering & Structural Dynamics* 2012; **42**(3):431–449.
41. Konstantinidis D, Makris N. Experimental and analytical studies on the response of 1/4-scale models of freestanding laboratory equipment subjected to strong earthquake shaking. *Bulletin of Earthquake Engineering* 2010; **8**(6): 1457–1477.
42. Oikonomou K, Roh H, Reinhorn AM, Schiff A, Kempner L. Seismic performance evaluation of high voltage transformer bushings. *In Structures Congress, ASCE* 2010. Joint NASCC & Structures Congress 2010, Orlando, Florida, USA MAY 12-15, 2010, Paper # 836, 2724-2735.
43. Dimitrakopoulos EG, Kappos AJ, Makris N. Dimensional analysis of yielding and pounding structures for records without distinct pulses. *Soil Dynamics and Earthquake Engineering* 2009; **29**(7):1170–1180.

DOI: 10.1002/eqe

44. Buckingham E. On physically similar systems; illustrations of the use of dimensional equations. *Physical Review* 1914; **4**(4):345–376.
45. Barenblatt GI. *Scaling, Self-similarity, and Intermediate Asymptotics: Dimensional Analysis and Intermediate Asymptotics*, Cambridge University Press: Cambridge, 1996.
46. Siano DB. Orientational analysis—a supplement to dimensional analysis—I. *Journal of The Franklin Institute* 1985; **320**(6):267–283.
47. Padgett JE, Nielson BG, DesRoches R. Selection of optimal intensity measures in probabilistic seismic demand models of highway bridge portfolios. *Earthquake Engineering & Structural Dynamics* 2008; **37**(5):711–725.
48. Cornell CA, Jalayer F, Hamburger RO, Foutch DA. Probabilistic basis for 2000 SAC federal emergency management agency steel moment frame guidelines. *Journal of Structural Engineering* 2002; **128**(4):526–533.
49. Gehl P, Seyedi DM, Douglas J. Vector-valued fragility functions for seismic risk evaluation. *Bulletin of Earthquake Engineering* 2013; **11**(2):365–384.
50. Diez DM, Barr CD, Cetinkaya-Rundel M. *OpenIntro Statistics*, 2012. CreateSpace independent publishing platform.
51. Baker J. Efficient analytical fragility function fitting using dynamic structural analysis. *Earthquake Spectra* 2013. in-press.

DOI: 10.1002/eqe